Advances in Geo-Energy Research

Vol. 20, No. 3, p. 213-226, 2026

Original article

Dynamic Mohr-Coulomb evaluation of natural fracture stability in deep shale under hydraulic fracturing induced stress superposition

Pengyu Liu, Cunqi Jia*

Physical Science and Engineering Division, King Abdullah University of Science and Technology, Thuwal 23955-6900, Saudi Arabia

Keywords:
Natural fracture
hydraulic fracturing induced stress
dynamic Mohr-Coulomb criterion
natural fracture risk zone
casing deformation

Cited as:
Liu, P., Jia, C. Dynamic Mohr-Coulomb evaluation of natural fracture stability in deep shale under hydraulic fracturing induced stress superposition. Advances in Geo-Energy Research, 2026, 20(3): 213-226.
https://doi.org/10.46690/ager.2026.06.04

Abstract:
Natural fractures affect hydraulic fracture propagation, pressure diffusion, casing integrity and stimulation efficiency in deep unconventional reservoirs. Conventional Mohr-Coulomb stability analysis usually assumes a fixed or weakly updated stress field, limiting its ability to capture evolving geomechanical perturbations during hydraulic fracturing. This study proposes a dynamic Mohr-Coulomb stability evaluation framework based on stress superposition induced by hydraulic fractures. Laboratory-constrained mechanical parameters, three-dimensional geomechanical modeling, induced stress redistribution and dynamic Mohr circle updating are integrated and tested using continental and marine shale cases. The results show that hydraulic fracturing increases all three principal stresses, with the minimum horizontal principal stress showing the strongest response. The effective stress superposition range is mainly limited to adjacent fracturing stages, indicating a localized but mechanically significant interaction zone. Static analysis reveals a nonlinear relationship between critical pore pressure increment and fracture approach angle, defining a friction-controlled stability window. Dynamic analysis further incorporates variations in principal stress, pore pressure, maximum horizontal stress orientation and fracture cohesion. The predicted activation risk zones agree with field observations from treatment pressure responses and microseismic data. Pumping rate optimization reduces activation risk by weakening stress and pore pressure perturbations near critically oriented natural fractures. The proposed framework provides a quantitative basis for diagnosing natural fracture activation, mitigating casing deformation and optimizing fracturing parameters in deep fractured shale reservoirs.

1. Introduction

Natural fractures exert a fundamental control on hydraulic fracturing effectiveness and subsequent production performance in shale oil and shale gas reservoirs (Cai et al., 2024). In the Yingxiongling area of the Qaidam Basin, China, shale oil reservoirs are characterized by complex structural settings (Liu et al., 2024b). During hydraulic stimulation, pre-existing discontinuities influence hydraulic-fracture trajectories, promote fluid leak-off, increase treatment complexity and elevate operational cost. During production, these reservoirs commonly exhibit high initial rates followed by rapid decline (Zhao et al., 2020; Yang et al., 2026). In the Sichuan Basin, China, deep shale gas reservoirs are intensively fractured. Field statistics indicate that the casing-deformation rate reaches approximately 51%, and the estimated ultimate recovery of wells with casing deformation is only about 70% of that of mechanically intact wells (Liu et al., 2019; Sun et al., 2024). Such deformation is primarily attributed to the activation and

Yandy Scientific Press

*Corresponding author.
E-mail address: Pengyu.liu@kaust.edu.sa (P. Liu); cunqi.jia@kaust.edu.sa (C. Jia).

Received April 14, 2026; revised May 11, 2026; accepted May 22, 2026; available online May 25, 2026.

shear slip of natural fractures induced by hydraulic fracturing, which compromises casing integrity (Liu et al., 2019; Han et al., 2023; Lei et al., 2024a). These field observations show that a quantitative stability-evaluation method for pre-existing discontinuities is essential for both stimulation design and long-term reservoir performance.

The interactions between hydraulic fractures and natural fractures can be broadly classified into three types: Hydraulic fractures that penetrate natural fractures, propagate along natural fractures, or activate natural fractures through hydraulic-fracture-induced stress perturbations (Hu and Ghassemi, 2021; Zhang et al., 2026). When hydraulic fractures intersect natural fractures, their propagation behavior is jointly controlled by multiple factors, including horizontal stress difference and stress ratio, fracture approach angle, cementation and frictional properties of natural fractures, pore-fluid pressure within fractures, injection rate, and fracturing-fluid viscosity (Sun et al., 2022; Tan et al., 2023). In cases where direct intersection does not occur, hydraulic fractures may still destabilize nearby natural fractures by modifying the local stress state through induced stress fields. Conversely, the activation or failure of natural fractures can alter hydraulic fracture propagation patterns (Shi et al., 2024).

During hydraulic fracture propagation, both the magnitude and orientation of the *in-situ* horizontal stresses evolve dynamically, with variations in the minimum horizontal principal stress generally exceeding those in the maximum horizontal principal stress (Ren et al., 2022; Lei et al., 2024b). Such stress perturbations can induce pore-pressure fluctuations within natural fractures, potentially triggering slip or opening. In formations characterized by high stress ratios, even natural fractures located at relatively large distances from hydraulic fractures may become unstable (Cao and Sharma, 2022). The stability of natural fractures under induced stress perturbations is governed by multiple parameters, including the orientation of the horizontal principal stresses, horizontal stress difference, fracture approach angle and distance, net fracture pressure, fracture closure state, and hydraulic fracture length (Dubinya, 2022; Teixeira Silveira et al., 2022). The spatial extent of the induced stress field generated by a single hydraulic fracture is further controlled by fracture height, net pressure, Poisson's ratio, and the ratio of maximum to minimum horizontal stresses, while stress superposition from multiple fractures additionally depends on fracture spacing and fracture number (Rocha and Wahrhaftig, 2016; Guan et al., 2019).

Previous studies have improved the understanding of hydraulic fracture and natural fracture interaction. However, many practical analyses still focus on static crossing, opening or slipping conditions. The spatial range of multi-stage stress superposition remains insufficiently quantified. In addition, the coupled evolution of principal stress, pore pressure and horizontal stress orientation has rarely been converted into an operational activation-risk map for field-scale fracturing design. To address these limitations, this study develops a dynamic Mohr-Coulomb stability evaluation workflow for natural fractures under hydraulic-fracture-induced stress superposition. The workflow integrates induced-stress superposition, pore-pressure updating, stress-orientation rotation and fracture cohesion into a spatial risk-zone mapping procedure. Continental shale and marine shale cases are used to examine the transferability of the method across different tectonic and sedimentary settings.

The specific contributions of this study are as follows. First, a quantitative threshold is used to define the effective spatial range of stress superposition induced by multi-stage hydraulic fracturing. Second, the Mohr stress circle is dynamically updated by incorporating changes in principal stress, pore pressure, maximum horizontal stress orientation and cohesion. Third, the predicted natural fracture activation-risk zones are examined using treatment pressure responses and microseismic observations. Through this workflow, hydraulic-fracture-induced stress and pressure perturbations are translated into a map-based stability criterion for identifying natural fracture activation risk and supporting adaptive optimization of fracturing parameters.

2. Methodology and geomechanical models

2.1 Natural fracture instability criterion

Hydraulic fracturing creates high-conductivity flow paths for hydrocarbon production in unconventional reservoirs. However, shale reservoirs commonly contain natural fractures that may be reactivated during stimulation. Their activation can complicate fracture propagation and lead to interwell communication, poor proppant placement, abnormal pressure decline and casing deformation. Natural fractures may lose stability either through direct intersection with hydraulic fractures or through remote stress and pore-pressure perturbations induced by hydraulic-fracture growth. This study focuses on the second mechanism, namely natural fracture activation without direct hydraulic-fracture intersection.

For the continental and marine shale cases examined in this study, the *in-situ* stress state can be approximated by a strike-slip faulting regime. In this regime, the maximum horizontal principal stress is the greatest principal stress, the vertical stress is the intermediate principal stress, and the minimum horizontal principal stress is the least principal stress. The stability of an inclined natural fracture is evaluated by resolving the far-field stress state onto the fracture plane. In the horizontal *x*-*y* plane, the normal stress σ and shear stress τ acting on a plane with an orientation angle θ, measured counterclockwise from the x axis, can be obtained from the two-dimensional stress transformation as follows (Xia et al., 2025):

$$\sigma = \frac{\sigma_x + \sigma_y}{2} + \frac{\sigma_x - \sigma_y}{2}\cos 2\theta - \tau_{xy}\sin 2\theta \tag{1}$$

$$\tau = \frac{\sigma_x - \sigma_y}{2}\sin 2\theta + \tau_{xy}\cos 2\theta \tag{2}$$

where σ denotes the normal stress, MPa; σ_x and σ_y denote the normal stresses along the *x*- and *y*-axes, respectively, MPa; θ is the angle of inclination, °; τ is the shear stress, MPa; τ_{xy} is the shear stress on the plane inclined by an angle θ, MPa.

Eqs. (1) and (2) can be simplified into the Mohr stress circle by utilizing trigonometric identities:

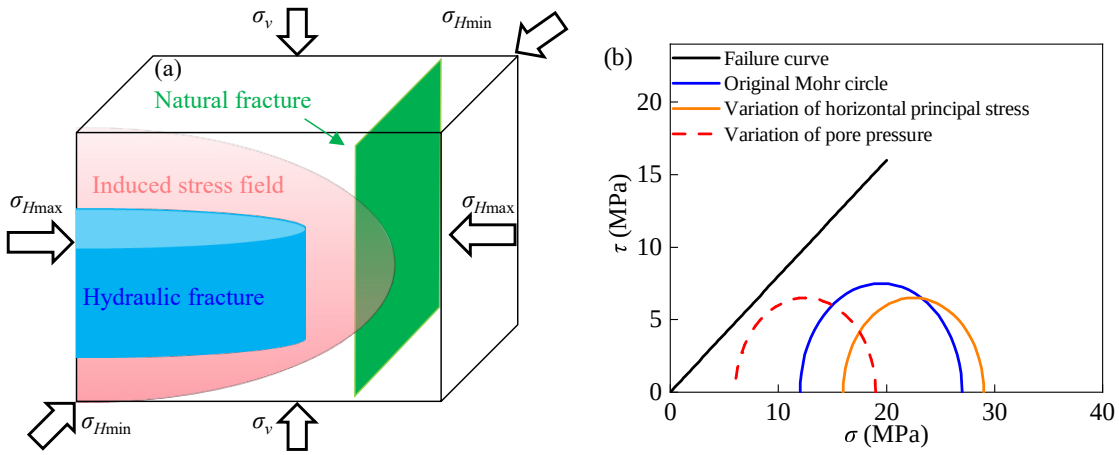

Fig. 1. Instability model of natural fractures based on dynamic Mohr stress circle: (a) Instability model of natural fractures and (b) dynamic Mohr stress circle.

$$\left(\sigma-\frac{\sigma_x+\sigma_y}{2}\right)^2+\tau^2=\left(\frac{\sigma_x-\sigma_y}{2}\right)^2+{\tau_{xy}}^2 \tag{3}$$

The shear instability of natural fractures based on the static Mohr-Coulomb criterion is expressed as follows (Zhang et al., 2003; Potluri et al., 2005):

$$\tau=C+\tan\varphi\,(\sigma-p) \tag{4}$$

where C is the cohesion, MPa; φ is the internal friction angle, °; p is the formation pressure, MPa.

The classical static Mohr-Coulomb criterion assumes an unchanged stress state. This assumption is inadequate during hydraulic fracturing. Fracture opening, net pressure, stress shadowing and interaction among adjacent stages continuously perturb the local stress field (Warpinski and Branagan, 1989; Palmer, 1993). These perturbations change both the center and radius of the Mohr stress circle. In multi-stage fracturing, induced stresses from different stages may overlap and further modify the stress state around hydraulic fractures and nearby natural fractures (Zeng and Guo, 2015).

When hydraulic fractures do not directly intersect natural fractures, natural fracture activation is mainly controlled by remote stress and pore-pressure perturbations, as shown in Fig. 1(a). Under hydraulic-fracture-induced stress loading, the three principal stresses around a natural fracture generally increase. This shifts the Mohr stress circle to higher normal stress. Because the increase in minimum horizontal principal stress is commonly greater than that in maximum horizontal principal stress, the diameter of the Mohr stress circle decreases. This stress change may have a stabilizing effect on shear slip. However, the increase in the three-dimensional stress state can also raise pore pressure within natural fractures. Higher pore pressure reduces the effective normal stress on the fracture plane and shifts the effective Mohr stress circle toward lower normal stress, as shown in Fig. 1(b). This process may partly offset the stabilizing effect of increased principal stresses. In this study, the pore-pressure response is estimated from the minimum horizontal principal stress, vertical stress and Poisson's ratio using Eq. (5) (Hillis, 2001). The calculated pore-pressure increment may exceed the corresponding increments in the principal stresses. Eq. (5) is used only as a first-order undrained poroelastic estimate of pore-pressure response to stress perturbation. It is not a transient pressure-diffusion solution for high-rate injection. Under high injection rates, strong permeability heterogeneity or non-equilibrium pressure diffusion, the actual pore-pressure field may deviate from this estimate. Therefore, treatment-pressure responses and microseismic observations are used as field constraints when interpreting the predicted activation-risk zones.

At this stage, the effective Mohr stress circle is recalculated using Eq. (6). Stress increments and pore-pressure increments have opposite effects on the effective stress state. An increase in principal stress shifts the Mohr stress circle toward higher normal stress, whereas an increase in pore pressure shifts the effective Mohr stress circle toward lower normal stress. Their coupled effects may activate natural fractures that remain stable under the initial static Mohr-Coulomb criterion. The dynamic calculation follows a stage-wise quasi-static procedure (Zhang and Yin, 2017):

$$P_p=\frac{\sigma_h-k\sigma_v}{1-k} \tag{5}$$

$$\left(\sigma-\frac{\sigma_H+\Delta\sigma_H+\sigma_h+\Delta\sigma_h}{2}+P_p+\Delta P_p\right)^2+\tau^2=\left(\frac{\sigma_H+\Delta\sigma_H-\sigma_h-\Delta\sigma_h}{2}\right)^2+{\tau_{xy}}^2 \tag{6}$$

where P_p is the pore pressure inside the fractures, MPa; ΔP_p is the pore pressure increment, MPa; σ_H is the maximum horizontal principal stress, MPa; $\Delta\sigma_H$ is the increment of maximum horizontal principal stress, MPa; σ_h is the minimum horizontal principal stress, MPa; $\Delta\sigma_h$ is the increment of minimum horizontal principal stress, MPa; σ_v is the overburden stress, MPa; k is the tectonically unperturbed stress coefficient.

2.2 Three-dimensional geomechanical model

To evaluate the transferability of the proposed stability workflow, two shale systems were selected: Continental shale

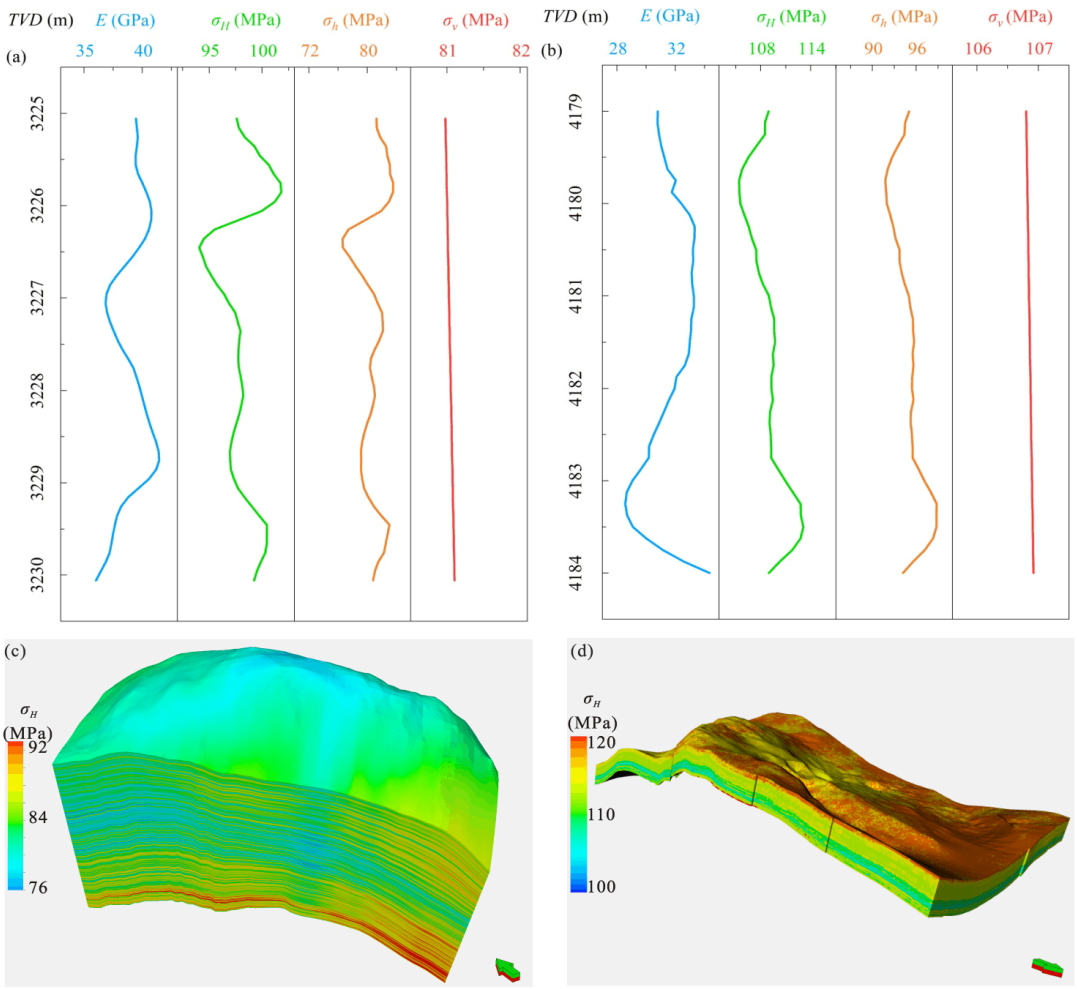

Fig. 2. Logging curves and numerical models of shale reservoirs: (a) Logging curves of continental shale, (b) logging curves of marine shale, (c) geomechanical model of continental shale and (d) geomechanical model of marine shale.

from the Yingxiongling area of the Qaidam Basin and marine shale from the Zigong area of the Sichuan Basin. The comparison was designed to test whether the stress perturbation based stability evaluation remains applicable under different depositional, mineralogical and structural conditions. The Yingxiongling shale was deposited in a lacustrine setting and was strongly modified by regional compression. It contains calcite, quartz and clay minerals, with pronounced lamination, bedding and lithological heterogeneity. These features reflect the combined effects of high frequency sedimentary cyclicity and tectonic deformation. In contrast, the Zigong marine shale is dominated by clay minerals and quartz and exhibits more uniform laminated structures.

Three-dimensional geomechanical models were constructed for both shale systems using the Petrel geomechanical workflow (Fig. 2). For the Qaidam Basin case, the target interval is located at a true vertical depth of 3,243-3,298 m. The average maximum horizontal principal stress is 92.1 MPa, the average minimum horizontal principal stress is 77.6 MPa, and the average vertical stress is 84.4 MPa. The horizontal stress difference is approximately 15 MPa. The elastic modulus derived from acoustic logs averages 39 GPa (Fig. 2(a)). For the Sichuan Basin case, the target interval occurs at a true vertical depth of 4,179-4,184 m. The average maximum horizontal principal stress, minimum horizontal principal stress and vertical stress are 109.8, 95.8 and 106.8 MPa, respectively. The horizontal stress difference is approximately 14 MPa, and the log derived elastic modulus averages 37 GPa (Fig. 2(b)). Although the two cases differ in burial depth and stress magnitude, their horizontal stress differences and elastic moduli are comparable. This makes them suitable for evaluating induced stress effects under different shale settings.

Based on log interpretation, three-dimensional stress models were built using the Quick Mechanical Earth Model workflow (Figs.2(c) and 2(d)). Elastic properties were first obtained from well logs. Static Young's modulus was then used to estimate uniaxial compressive strength and tensile strength. These parameters, together with internal friction angle, were used to construct the rock strength model. The *in-situ* stress field was calculated by integrating rock strength, bulk density, pore pressure and elastic property models. Natural fracture networks interpreted from ant tracking seismic discontinuity attributes were then embedded into the geomechanical models. The resulting models provide the stress field, rock strength and

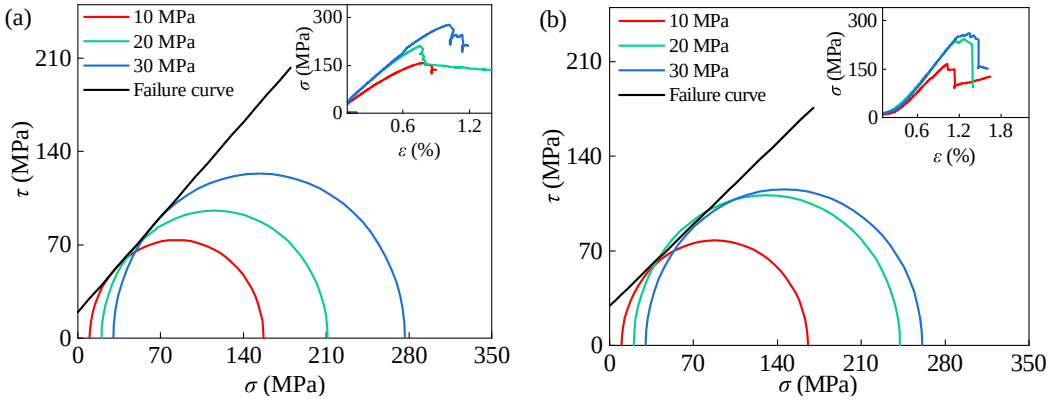

Fig. 3. Results of rock mechanics experiments: (a) Mohr stress circle of continental shale and (b) Mohr stress circle of marine shale.

fracture geometry required for induced stress simulation and natural fracture stability evaluation.

For stress superposition and activation-risk mapping, the Petrel geomechanical models were exported as corner point grids. The grids were resampled to approximately 10 m × 10 m in the horizontal direction, with 1-2 m vertical layering in the target interval. Far-field horizontal stress constraints were applied to the lateral boundaries. The lower boundary was fixed in the normal direction, and the upper boundary was loaded by overburden stress derived from density log integration. Initial pore pressure and the three principal stresses were obtained from the log constrained mechanical earth model. For each shale case, the same initial stress field was used across the comparative simulations to isolate the effect of stage-by-stage stress superposition.

In the UFM simulations, hydraulic fractures were represented as vertical and height limited fractures. Local deviation was allowed under stress shadow interaction. Fracture geometry was controlled by the field stage design, cluster spacing, pumping rate, fluid intensity and proppant intensity. During calibration, net pressure was constrained to 6-12 MPa for the continental shale and 7-14 MPa for the marine shale. Leakoff was described using a Carter type model, with consistent leakoff parameters across the comparative cases. A time step of 0.5 min was used. Stress field outputs were exported after each stage for activation-risk analysis. The stochastic parameters controlling cluster efficiency, local propagation disturbance and fracture height variability were kept constant in the one-stage, two-stage, three-stage and four-stage simulations. Therefore, the differences among these cases mainly reflect the number and configuration of adjacent stages.

3. Dynamic responses to hydraulic-fracture-induced stress fields

3.1 Laboratory rock mechanical properties

The Yingxiongling continental shale is a typical mixed shale with well-developed lamination and strong lithological heterogeneity (Liu et al., 2024a, 2024b). In contrast, the Zigong marine shale has a relatively simple mineral composition and more continuous bedding structures. Representative samples from both shale systems were tested to obtain rock mechanical parameters for constraining the geomechanical model. Because lamination intensity and lithological heterogeneity vary within the Yingxiongling shale, its mechanical properties show sample-scale variability. To reduce this effect, triaxial compression tests were conducted on samples from target intervals with similar burial depth, physical properties and mechanical characteristics. Two groups of triaxial tests were performed for each shale type to improve parameter reliability. Based on the measured peak strengths under different confining pressures, Mohr stress circles and Mohr-Coulomb failure envelopes were constructed, as shown in Fig. 3.

The measured elastic modulus of both shale types increases with confining pressure. The Mohr-Coulomb failure envelopes derived from triaxial compression tests give an average cohesion of 20.8 MPa and an internal friction angle of 44.8° for the Yingxiongling continental shale. The corresponding values for the Zigong marine shale are 19.3 MPa and 46.7°. For the natural fracture stability charts, discontinuity-scale effective friction coefficients of 0.9 and 0.8 were assigned to the continental and marine shale cases, respectively. These coefficients are constrained by the laboratory failure envelopes and published shale fracture-friction ranges. They should not be interpreted as direct shear measurements on individual natural fracture surfaces. This distinction is necessary because the cohesion and frictional resistance of pre-existing discontinuities are generally lower and more uncertain than those of intact shale matrix.

Although the two shale systems have broadly comparable strength parameters, their stress-strain responses differ. The marine shale shows a longer initial fracture-closure stage, indicating more developed bedding planes and microfractures that can close and reopen during loading. The continental shale shows a more compact mechanical response, probably due to stronger cementation. Its post-elastic stress-strain curves display marked nonlinearity, suggesting that mixed mineral composition and laminar fabric promote nonlinear deformation and limited plastic accommodation. These laboratory constrained parameters provide calibrated inputs for induced stress

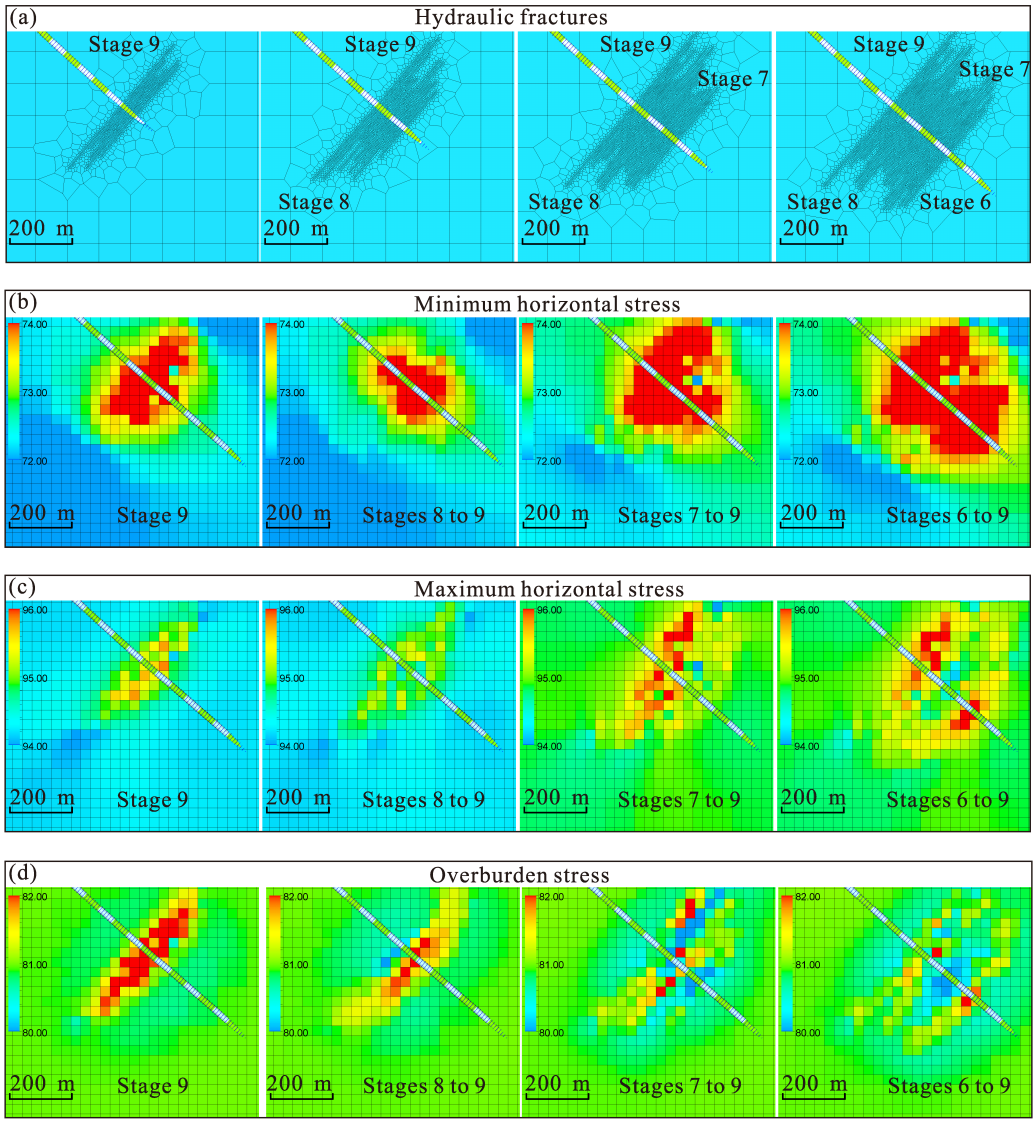

Fig. 4. Numerical simulation results of the three-dimensional stress field for hydraulic fracturing in continental shale: (a) Hydraulic fractures, (b) minimum horizontal principal stress, (c) maximum horizontal principal stress and (d) vertical stress.

simulation and natural fracture stability evaluation.

3.2 Hydraulic fracture-induced stress field results

Numerical simulations were performed using Petrel and the Unconventional Fracture Model to evaluate hydraulic fracture induced stress redistribution in the continental and marine shale reservoirs. The models were constrained by laboratory derived rock mechanical parameters and log based geomechanical properties. A sequential workflow was used. Hydraulic fracture propagation and induced stress fields were simulated first, and the updated stress outputs were then used for dynamic Mohr-Coulomb evaluation of natural fracture stability. This workflow allows field scale multi-stage analysis while reducing the influence of stochastic fracture propagation on the interpretation of induced stress effects.

For the continental shale model, the initial maximum horizontal stress, minimum horizontal stress and vertical stress were 94.84 MPa, 72.36 and 80.96 MPa, respectively, with a pore pressure of 54.71 MPa. The maximum-horizontal-stress azimuth was 40.47° east of north. The horizontal well had a lateral length of 1,528 m and was designed with 27 stages and 155 clusters, with a cluster spacing of 7.5 m and an inter-stage spacing of 15.5 m. Based on field operation data, the pumping rate, fluid intensity and proppant intensity were 16, 26 and 2.7 $m^3 \cdot m^{-1}$, respectively.

The simulated stress fields show that hydraulic-fracture propagation produces a clear redistribution of the triaxial stress field (Fig. 4). In the single-stage case, fractures at the two sides of the stage propagate farther, whereas fractures in the central region are shorter because of inter-cluster stress shadowing. The principal stresses decrease near fracture tips but increase around fracture bodies and along the wellbore direction. Among the three principal stresses, the minimum horizontal stress exhibits the largest affected range, indicating

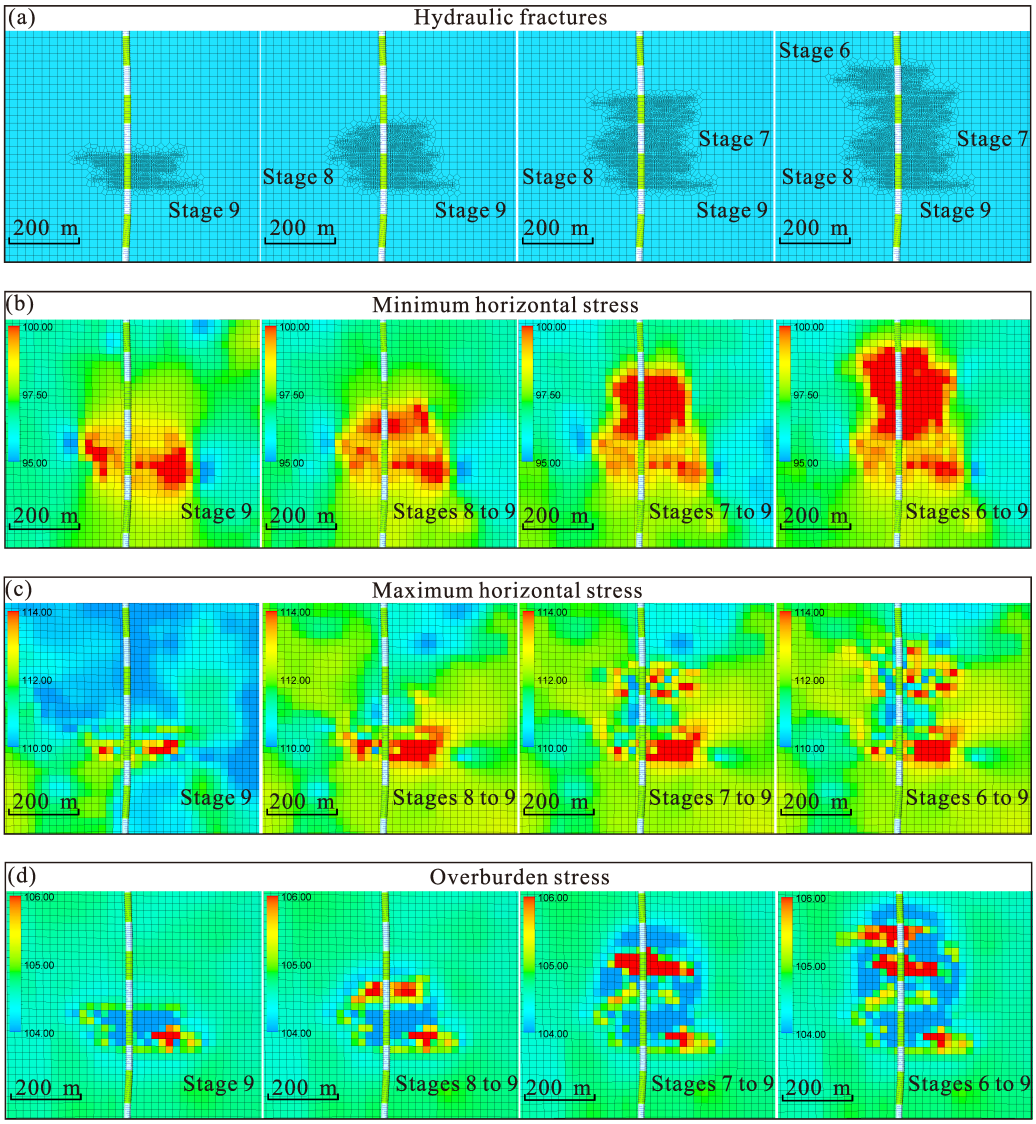

Fig. 5. Numerical simulation results of the three-dimensional stress field for hydraulic fracturing in marine shale: (a) Hydraulic fractures, (b) minimum horizontal principal stress, (c) maximum horizontal principal stress and (d) vertical stress.

that it is the most sensitive component to hydraulic-fracture-induced stress perturbation. In the two-stage case, the fracture length of Stage 9 decreases on the side adjacent to Stage 8 and increases on the opposite side, reflecting the combined effects of stress shadowing and adjacent-stage stress superposition. The three-stage and four-stage cases show similar stress-interaction patterns, suggesting that the induced-stress superposition effect tends to converge as the number of adjacent stages increases.

The marine shale model has a maximum horizontal principal stress of 109.5 MPa, a minimum horizontal principal stress of 94.4 MPa, a vertical stress of 105.6 MPa, a pore pressure of 87.2 MPa, and an east-west maximum-horizontal-stress orientation. A single horizontal well model was constructed based on the field fracturing design, with a horizontal section length of 1805 m. An extended-stage multi-cluster design was adopted, comprising 23 stages and 299 clusters, with a cluster spacing of 5.8 m and a stage spacing of 83.2 m. Using actual field operation data, a multi-stage diverter fracturing scheme was simulated, with a pumping rate of 18 $m^3 \cdot min^{-1}$, a fluid intensity of 30.6 $m^3 \cdot m^{-1}$, and a proppant intensity of 2.7 $m^3 \cdot m^{-1}$. For comparison, Stage 9 was selected as the reference stage (Fig. 6). Because each marine-shale stage contains 13 clusters, inter-cluster stress shadowing is more pronounced. Consistent with the continental-shale results, all three principal stresses decrease near fracture tips and increase around fracture bodies and toward the wellbore, with the minimum horizontal principal stress showing the largest affected zone.

3.3 Hydraulic fracture propagation results

To evaluate the effect of induced stress superposition on hydraulic fracture propagation, fracture lengths of different clusters were compared under different numbers of adjacent stages in both shale cases. In the continental shale, Cluster 1, which is farthest from Stage 8, has the longest fracture length, whereas Cluster 6, which is closest to Stage 8, has

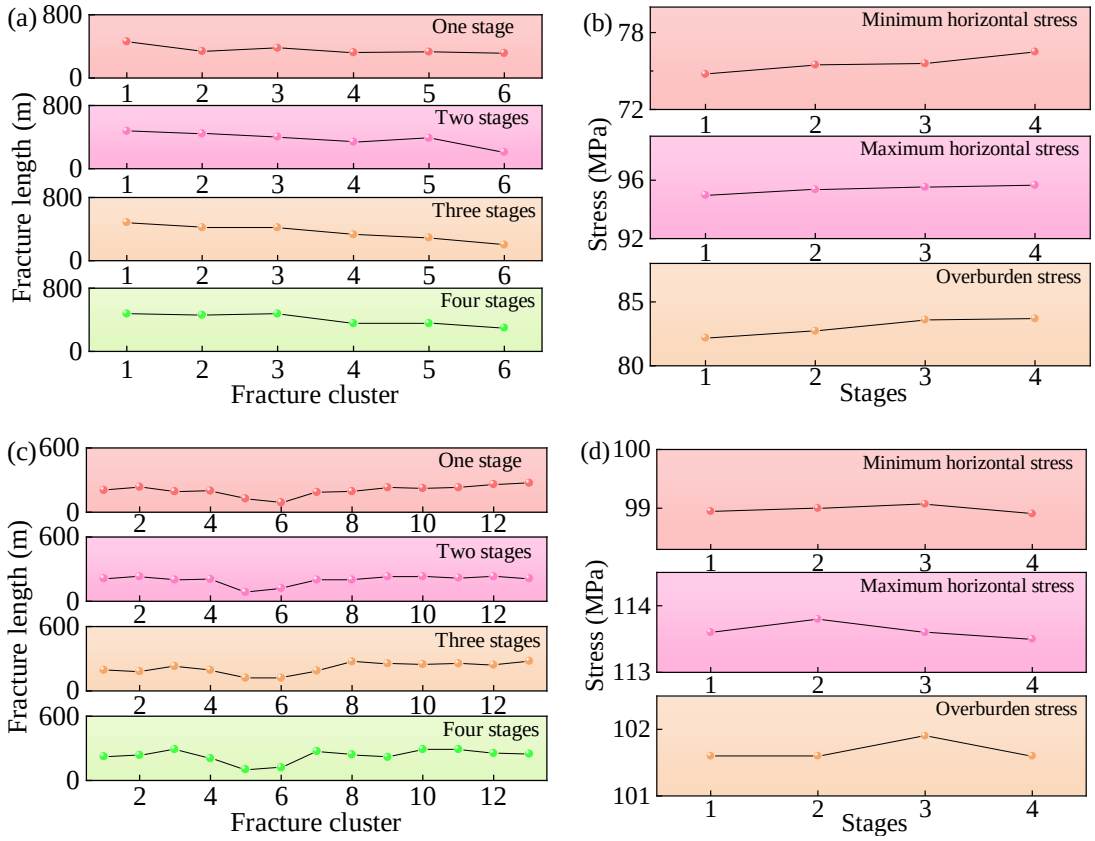

Fig. 6. Results of induced stress fields with different numbers of stages: (a) Hydraulic fracture lengths of Stage 9 in continental shale, (b) three principal stress values at the fracture center of Stage 9 in continental shale, (c) hydraulic fracture lengths of Stage 9 in marine shale and (d) three principal stress values at the fracture center of Stage 9 in marine shale.

the shortest fracture length (Fig. 6(a)). As more adjacent stages are included, the fracture lengths of Clusters 4 and 5 decrease, indicating stronger stress shadowing and induced stress superposition. The three principal stresses at the center of Stage 9 fractures also increase with the number of adjacent stages (Fig. 6(b)). In the three stage and four stage cases, both fracture length and principal stress tend to stabilize. This suggests that the propagation of Stage 9 is mainly controlled by the nearest three adjacent stages, whereas more distant stages have a limited additional effect.

In the marine shale, the larger number of clusters per stage distributes stress interaction among more fractures. As a result, the influence on Clusters 5 and 6 lasts for a shorter distance or duration. The fracture length of Cluster 13 in Stage 9 decreases because of stress interaction from preceding stages. Similar to the continental shale case, fracture lengths and principal stresses become nearly stable in the three stage and four stage simulations (Figs. 6(c) and 6(d)). This result indicates that the effective range of induced stress superposition is spatially limited in both shale systems.

For the shale reservoirs examined in this study, the effective range of hydraulic fracture induced stress superposition was mainly limited to the nearest three adjacent stages. This range was defined using a 5% mechanical threshold. An additional stage was considered significant only when it changed either the principal stress at the fracture center or the representative cluster fracture length by more than 5% relative to the previous stage configuration. Under this criterion, the difference between the three stage and four stage cases was below 5% for both fracture length and principal stress. For Stage 9, the farthest effective contribution was therefore from Stage 6. This indicates that the local dynamic stress state was mainly controlled by Stages 6 to 8. The subsequent stability analysis can therefore focus on the dominant adjacent stage stress sources rather than the full stimulation history.

A local sensitivity analysis was conducted around the Stage 9 model to test the robustness of this influence range. Stage spacing, cluster spacing and fracture half length were varied by ±25% relative to the base case. Net pressure was tested within 6 to 14 MPa. Pumping rate ranged from 14 to 20 $m^3 \cdot min^{-1}$, and Young's modulus ranged from 30 to 45 GPa. Smaller stage spacing, smaller cluster spacing, longer fracture half length, higher net pressure and higher pumping rate increased induced stress perturbation and enlarged the local activation risk zone. A higher Young's modulus reduced deformation compliance and slightly weakened fracture length variation caused by stress shadowing. Despite these amplitude changes, the fourth adjacent stage generally produced changes below the 5% threshold. Therefore, the three stage range should be interpreted as an operationally effective influence range

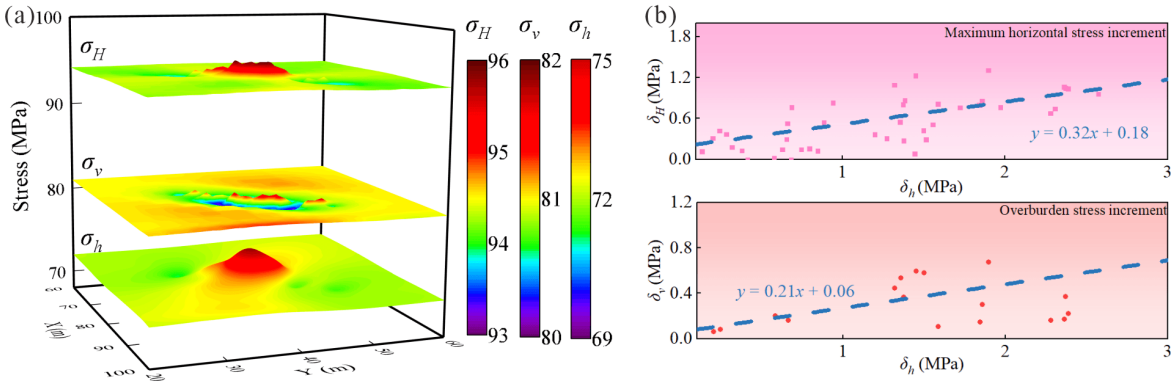

Fig. 7. Induced principal stress distribution and stress increment relationships in Stage 9: (a) Spatial distribution of the maximum horizontal stress, overburden stress and minimum horizontal stress and (b) linear relationships among principal stress increments.

under the tested geological and engineering conditions, not as a universal geometric rule. For reservoirs with shorter stage spacing, longer hydraulic fractures or higher net pressure, the same threshold criterion should be reapplied.

The induced stress field around Stage 9 was further analyzed to identify the most sensitive stress component. Under the influence of Stages 6 to 8, both the maximum and minimum horizontal principal stresses increased within the hydraulic fracture region. Low stress zones developed near fracture tips. The minimum horizontal principal stress showed the largest increase and the widest affected area. The vertical stress also increased around the hydraulic fractures (Fig. 7(a)). After excluding fracture tip low stress zones, the maximum horizontal stress and vertical stress showed positive correlations with the minimum horizontal stress. This indicates a coordinated triaxial stress response controlled by fracture opening and stress shadowing. The minimum horizontal stress can therefore be used as a sensitive indicator for identifying zones where the effective Mohr stress circle is strongly modified (Fig. 7(b)).

Hydraulic fracture propagation also changed the maximum horizontal stress orientation. The initial maximum horizontal stress azimuth was 40.47° east of north. After fracture propagation, the stress orientation decreased in the northern and southern regions but increased in the eastern and western regions. This pattern caused an overall northward deflection of the hydraulic fractures. Although the angular change was small, it can modify the resolved normal and shear stresses on natural fracture planes. Stress orientation rotation should therefore be included in the dynamic stability evaluation of natural fractures.

In actual field development, wells commonly undergo multiple fracturing stages with short time intervals between stages. The finding that induced-stress superposition is mainly controlled by the nearest three stages has direct computational and operational significance. It reduces the number of stress sources that must be considered in real-time stability evaluation, shortens calculation time, and enables rapid updating of natural-fracture risk zones during field operations. This result also provides a physical basis for adaptive stage-spacing, cluster-spacing, and pumping-rate optimization.

4. Discussion based on the dynamic Mohr-Coulomb criterion

4.1 Stability analysis of natural fractures

In the initial reservoir state, natural fractures are governed by the combined effects of the maximum horizontal stress, minimum horizontal stress, vertical stress and pore pressure. For a vertical natural fracture with an approach angle α relative to the maximum-horizontal-stress direction, the normal and shear stresses acting on the fracture plane are given by (Liu et al., 2019; Han et al., 2023):

$$S_n = \frac{\sigma + \sigma_3 - (\sigma_1 - \sigma_3)\cos 2\alpha}{2} \tag{7}$$

$$\tau_{xy} = \frac{(\sigma_1 - \sigma_3)\sin 2\alpha}{2} \tag{8}$$

where S_n is the normal stress on the natural fracture plane, MPa; σ_1 is the maximum principal stress, MPa; σ_3 is the minimum principal stress, MPa; α is the fracture approach angle, °.

The effective normal stress of the fracture surface is:

$$\sigma_n = S_n = P_p \tag{9}$$

where σ_n is the effective normal stress on the fracture plane, MPa.

According to Amonton's friction law, when the friction coefficient is specified, a natural fracture becomes unstable if the resolved shear stress exceeds the frictional resistance on the fracture surface:

$$\tau_{xy} \geq \mu\sigma_n \tag{10}$$

where μ is the friction coefficient.

Under the static Mohr-Coulomb criterion, the total stress state is assumed to remain unchanged. Pore-pressure increase therefore directly reduces the effective normal stress and weakens frictional resistance. Substituting Eqs. (7)-(10) into the Coulomb limiting condition, $\tau = \mu\sigma_n + C$ and assuming zero cohesion yields the critical pore-pressure increment required for slip:

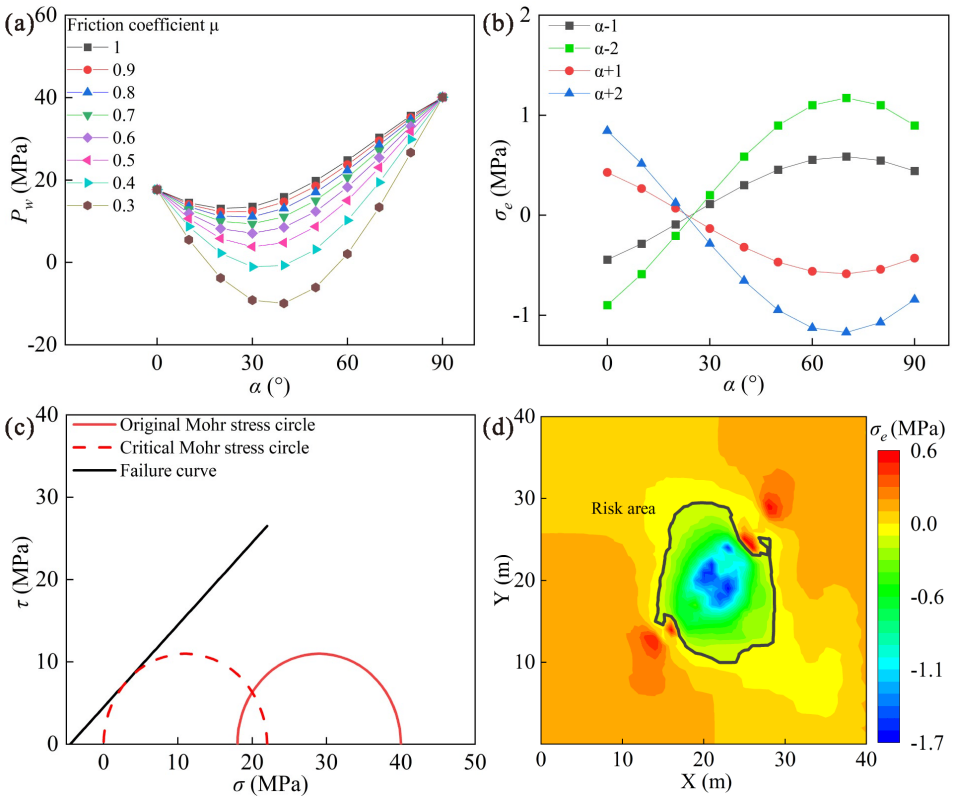

Fig. 8. Influencing factors of the dynamic Mohr circle: (a) Critical pore pressure increment template, (b) fracture approach angle and critical effective stress, (c) effect of cohesion on the Mohr stress circle and (d) natural fracture risk zone.

$$P_w = \sigma_3 - P_0 + (\sigma_1 - \sigma_3)\left(\sin^2\alpha - \frac{\sin\alpha\cos\alpha}{\mu}\right) \tag{11}$$

where P_w is the critical pore pressure increment, MPa; P_0 is the initial pore pressure, MPa.

For the continental shale case, the initial maximum horizontal stress, minimum horizontal stress, vertical stress and pore pressure are 94.84, 72.36, 80.96 and 54.71 MPa, respectively. The static stability envelope shows that the critical pore pressure increment first decreases and then increases with fracture approach angle, indicating that slip is favored only within a limited orientation range. When the friction coefficient is 0.4, fractures with approach angles of 26° to 42° are already unstable under the initial stress state. The critical friction coefficient is approximately 0.42. As the friction coefficient increases to 0.9, the most sensitive approach angle remains within 24° to 34°. Thus, the static envelope identifies frictional and orientational conditions favorable for reactivation, but it cannot account for hydraulic fracture induced stress evolution (Fig. 8(a)).

During hydraulic fracturing, fracture opening, net pressure, stress shadowing and interstage interaction modify the Mohr stress circle. Increased principal stresses shift the circle toward higher normal stress, while a larger increase in minimum horizontal stress reduces differential stress and may suppress shear slip. In contrast, pore pressure increase lowers effective normal stress and moves the effective Mohr stress circle toward failure. Sensitivity analysis under representative Yingxiongling conditions shows that pore pressure increase and cohesion reduction directly enhance slip tendency, whereas stress strengthening, especially the increase in minimum horizontal stress, has a stabilizing effect. Rotation of the maximum horizontal stress also changes the resolved normal and shear stresses when the fracture orientation is near the critical approach angle. Therefore, natural fracture reactivation is controlled by the combined effects of pore pressure weakening, cohesion loss, stress strengthening and stress orientation rotation. Based on a two dimensional plane stress approximation, the effect of stress rotation can be included by updating the effective fracture approach angle, and the critical effective stress increment is expressed as follows:

$$\alpha = \frac{1}{2}\left\{\tan^{-1}\left[\left(\frac{1}{2} - \frac{\sigma_e - \sigma_3 + P_0}{\sigma_1 - \sigma_3}\right)\frac{2\mu}{\sqrt{\mu^2+1}}\right] - \tan^{-1}\mu\right\} \tag{12}$$

where σ_e is the critical effective stress increment, MPa.

Natural fracture stability depends on both principal stress magnitudes and stress orientation. Therefore, the rotation of the maximum horizontal stress was included in the stability analysis. As shown in Fig. 8(b), hydraulic fracturing induces a maximum horizontal stress rotation of about 1° to 2°. This small rotation can still change the resolved normal and shear stresses on a natural fracture plane. Depending on fracture orientation, a 1° rotation can change the critical effective stress by more than 1 MPa, and a 2° rotation can produce a change greater than 2 MPa. Thus, stress orientation rotation should

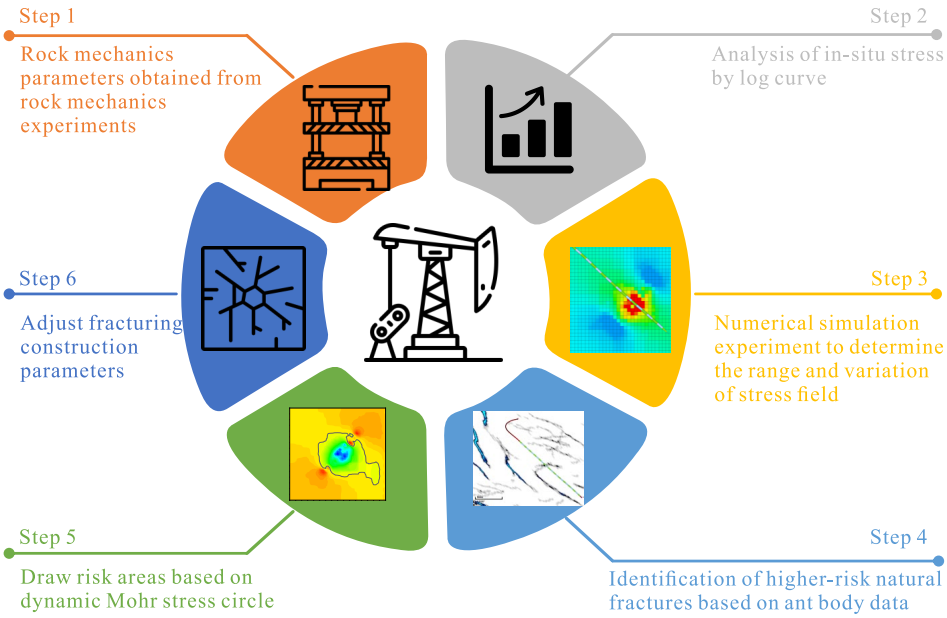

Fig. 9. Dynamic response analysis workflow for natural fracture stability.

be considered for fractures close to the static critical approach angle.

Cohesion was further examined as a sensitivity parameter. In natural fracture stability analysis, cohesion is commonly set to zero because pre-existing discontinuities may be weakened by mineral filling, cement degradation or previous shear displacement. For the Yingxiongling shale, with a friction coefficient of 0.9 and a horizontal stress difference of 22.48 MPa, the critical cohesion is approximately 4.5 MPa (Fig. 8(c)). This value was not used as the actual cohesion of natural fractures. It was used only to identify the transition in failure mode. When cohesion is lower than 4.5 MPa, shear slip is favored. When cohesion exceeds this threshold, tensile-shear failure becomes more likely.

Based on this interpretation, zero cohesion was used in the static stability assessment and dynamic risk-zone calculation to obtain a conservative estimate of natural fracture reactivation. With zero cohesion, a friction coefficient of 0.9 and an approach angle of 30°, the zero critical effective stress contour was defined as the boundary of the reactivation risk zone. Natural fractures inside this boundary are predicted to become unstable under hydraulic fracture induced stress perturbation. This treatment converts the Mohr-Coulomb criterion from a point-scale slip condition into a spatial diagnostic map for field-scale natural fracture stability evaluation (Fig. 8(d)).

4.2 Field-scale hydraulic fracturing of shale: A case study

This study establishes a field-scale workflow for evaluating natural fracture stability by coupling hydraulic fracture induced stress superposition with dynamic Mohr-Coulomb analysis (Fig. 9). The workflow consists of five steps. First, laboratory rock mechanical tests provide uniaxial compressive strength, elastic modulus, Poisson's ratio, cohesion and internal friction angle. These parameters constrain the geomechanical model and the failure criterion. Second, well logs and geomechanical modeling are used to determine the magnitude and orientation of *in-situ* stresses. Third, hydraulic fracture simulation is performed to quantify triaxial stress perturbation, maximum horizontal stress rotation, pore pressure response and the effective range of induced stress superposition. Fourth, natural fracture geometry and orientation within the affected zone are extracted from seismic and subsurface data. Finally, dynamic Mohr-Coulomb calculation is used to delineate natural fracture reactivation risk zones.

The workflow provides a map-based stability evaluation method for field-scale fracturing design. Before stimulation, it can be used to identify high-risk natural fracture corridors. During design, it can support stage placement, cluster spacing optimization and pumping-rate adjustment. During field operations, treatment pressure and microseismic responses can be used to check the predicted risk zones. For shale oil reservoirs, this approach helps identify zones where premature natural fracture activation may cause fluid loss or poor proppant placement. For deep shale gas reservoirs, it can support casing-deformation risk mitigation associated with unstable natural fractures. Therefore, the workflow links dynamic fracture stability evaluation with operational optimization of hydraulic fracturing.

The Yingxiongling continental shale case was used to validate the workflow shown in Fig. 9. As shown in Fig. 10(a), a natural fracture with an approach angle of about 30° is located within the predicted reactivation risk zone. The treatment-pressure curve shows that the operating pressure reached a turning point at about 77 min during continuous proppant injection and then began to decline (Fig. 10(b)). Microseismic monitoring shows relatively stable hydraulic fracture propagation during the early stage of treatment (Fig.

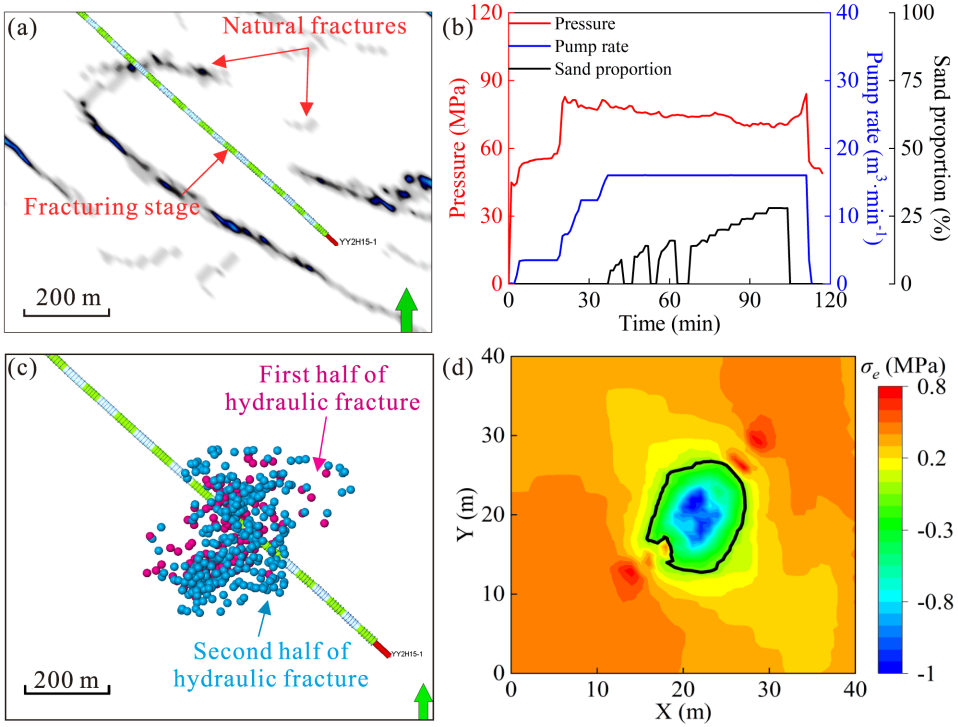

Fig. 10. Field example of natural-fracture instability risk assessment in continental shale: (a) Ant-tracking attributes, (b) fracturing treatment curve of Stage 9, (c) microseismic data of Stage 9 and (d) optimized natural-fracture risk zone.

10(c)). In the later stage, microseismic events increased markedly and clustered near Target A. The pressure decline and microseismic clustering occurred at nearly the same time, suggesting activation of a natural fracture and the formation of an additional pressure-dissipation pathway. By integrating the treatment-pressure response, microseismic distribution and predicted reactivation risk zone, the natural fracture in Fig. 10(a) is inferred to have become unstable during Stage 9 stimulation.

To reduce the predicted reactivation risk, the pumping rate was decreased from 16 to 14 $m^3 \cdot min^{-1}$, and hydraulic fracture propagation was re-simulated. The optimized risk zone is shown in Fig. 10(d). Compared with the original case at 16 $m^3 \cdot min^{-1}$, the reduced-rate case shows a smaller reactivation risk zone. This indicates that lowering the pumping rate can weaken hydraulic fracture induced stress and pore-pressure perturbations near critically oriented natural fractures. The result suggests that the dynamic stability workflow can support both post-treatment diagnosis and pumping-rate optimization.

The marine shale case provides an additional test of the dynamic stress based method for identifying natural fracture reactivation risk zones. At a pumping rate of 18 $m^3 \cdot min^{-1}$, the predicted risk zone shows a relatively large and continuous distribution in the hydraulically disturbed region (Fig. 11(a)). This pattern indicates that higher pumping rate enhances induced stress and pore pressure perturbations near the wellbore, causing more natural fractures to approach the critical slip condition. After the pumping rate is reduced to 16 $m^3 \cdot min^{-1}$, the predicted risk zone becomes smaller and less continuous (Fig. 11(b)). This result suggests that rate reduction can lower the probability of natural fracture reactivation and reduce the chance of hydraulic fracture communication with pre-existing discontinuities. Similar responses are observed in the continental shale case. Therefore, natural fracture reactivation is controlled not only by shale type, but also by the combined effects of induced stress perturbation, pore pressure variation, fracture orientation and frictional strength. For the tested continental and marine shale cases, the same dynamic stability workflow can be used to evaluate natural fracture reactivation risk and guide pumping rate optimization during hydraulic fracturing. This conclusion should be interpreted within the geological and engineering conditions examined in this study.

Pumping-rate reduction involves a clear engineering trade-off. A lower rate can reduce natural fracture reactivation risk by weakening induced stress and pore-pressure perturbations. However, it may also limit fracture length, height growth, fracture-network complexity and near-wellbore transport capacity. Reduced flow velocity may further weaken proppant transport and placement, which can decrease fracture conductivity, stimulated reservoir volume and estimated ultimate recovery. Therefore, rate reduction should not be treated as a general solution. It should be used as a constrained optimization strategy that balances natural fracture risk control with sufficient fracture geometry and proppant placement.

From a field-engineering perspective, avoiding hydraulic communication with critically oriented natural fractures may be more important than maximizing fracture complexity alone. Once hydraulic fractures connect with such discontinuities, casing deformation, fracture reactivation, interwell interference, pressure channeling and uncontrolled fluid migration

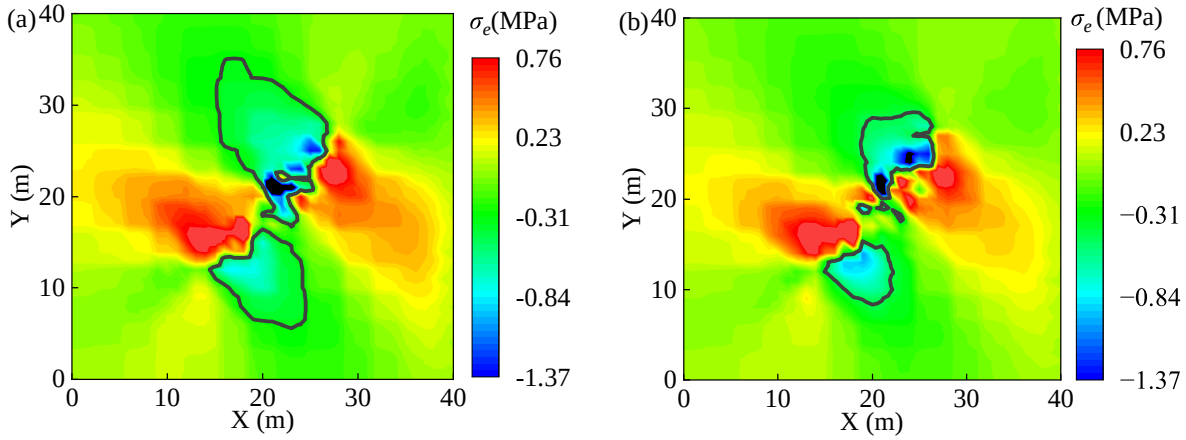

Fig. 11. Field example of natural-fracture instability risk assessment in marine shale: (a) Original natural-fracture risk zone and (b) optimized natural-fracture risk zone.

may occur. These responses can threaten well integrity and field-scale development safety. Therefore, the proposed workflow can support both fracturing design and field operation. During design, it can be used to adjust pumping rate, stage placement and cluster spacing when high-risk natural fractures are identified near the wellbore. During operation, treatment-pressure response, pressure fluctuation and microseismic activity can be used to update the risk interpretation and adjust the pumping rate. This allows hydraulic fracture extension to be controlled while reducing the probability of connection with high-risk natural fractures.

5. Conclusions

This study evaluated natural fracture stability in continental and marine shale reservoirs using a dynamic Mohr-Coulomb framework constrained by laboratory tests, geomechanical modeling, hydraulic fracture simulation and field monitoring. The main conclusions are as follows:

1) Hydraulic fracture propagation increases the triaxial stress around fractures and modifies the maximum horizontal stress orientation. Among the three principal stresses, the minimum horizontal principal stress shows the largest response. Using a 5% threshold in fracture center principal stress or representative cluster length, the effective range of multi-stage stress superposition is mainly limited to the nearest three adjacent stages in the tested shale cases.
2) The static Mohr-Coulomb analysis defines a baseline stability envelope for natural fractures. The critical pore pressure increment first decreases and then increases with fracture approach angle. This indicates that natural fracture slip is most likely within a finite orientation window, rather than across all fracture orientations.
3) Dynamic natural fracture stability is controlled by the coupled effects of principal stress variation, pore pressure increase, maximum horizontal stress rotation, cohesion and friction coefficient. Sensitivity analysis shows that pore pressure increase and cohesion reduction directly promote slip, whereas the increase in minimum horizontal principal stress tends to suppress slip by reducing differential stress. Stress orientation rotation becomes important when the fracture orientation is close to the critical approach angle.
4) A field scale workflow was established to convert hydraulic fracture induced stress and pressure perturbations into natural fracture reactivation risk zones. The Yingxiongling case shows that the predicted risk zone is consistent with pressure decline and microseismic event clustering during stimulation. Pumping rate reduction can contract the predicted risk zone, but it should be used as a constrained optimization strategy to balance natural fracture risk control, fracture geometry, proppant placement and stimulation effectiveness.

Acknowledgements

The authors gratefully acknowledge the continuous baseline funding provided by King Abdullah University of Science and Technology.

Conflicts of interest

The authors declare no competing interest.

References

Cai, J., Jiao, X., Wang, H., et al. Multiphase fluid-rock interactions and flow behaviors in shale nanopores: A comprehensive review. Earth-Science Reviews, 2024, 257: 104884.

Cao, M., Sharma, M. M. The impact of changes in natural fracture fluid pressure on the creation of fracture networks. Journal of Petroleum Science and Engineering,

2022, 216: 110783.

Dubinya, N. V. Spatial orientations of hydraulically conductive shear natural fractures for an arbitrary stress state: An analytical study of governing geomechanical factors. Journal of Petroleum Science and Engineering, 2022, 212: 110288.

Guan, B., Li, S., Liu, J., et al. Analysis and optimization of multiple factors influencing fracturing induced stress field. Journal of Petroleum Exploration and Production Technology, 2019, 10(1): 171-181.

Han, L., Li, X., Liu, Z., et al. Influencing factors and prevention measures of casing deformation in deep shale gas wells in Luzhou block, southern Sichuan Basin, SW China. Petroleum Exploration and Development, 2023, 50(4): 853-861.

Hillis, R. R. Coupled changes in pore pressure and stress in oil fields and sedimentary basins. Petroleum Geoscience, 2001, 7(4): 419-425.

Hu, L., Ghassemi, A. Laboratory-scale investigation of the slippage of a natural fracture resulting from an approaching hydraulic fracture. Rock Mechanics and Rock Engineering. 2021, 54: 2547–2558.

Lei, Q., Zhang, J., Zhu, X., et al. Experimental study on shear deformation mechanism and mitigation in shale gas casing. Engineering Failure Analysis, 2024a, 159: 108056.

Lei, Z., Wang, Z., Mu, L., et al. A technique for enhancing tight oil recovery by multi-field reconstruction and combined displacement and imbibition. Petroleum Exploration and Development, 2024b, 51(1): 137-146.

Liu, G., Wu, S., Wu, K., et al. Characteristics and hydrocarbon accumulation model of Paleogene whole petroleum system in western depression of Qaidam Basin, NW China. Petroleum Exploration and Development, 2024a, 51(5): 951-961.

Liu, K., Taleghani, A. D., Gao, D. Calculation of hydraulic fracture induced stress and corresponding fault slippage in shale formation. Fuel, 2019, 254: 115525.

Liu, P., Shen, Y., Gao, Y., et al. Laboratory study of stress sensitivity characterization and reservoir quality evaluation of Yingxiongling shale in Qaidam Basin. Energy & Fuels, 2024b, 38(7): 5822-5833.

Liu, K., Taleghani, A. D., Gao, D. Calculation of hydraulic fracture induced stress and corresponding fault slippage in shale formation. Fuel, 2019, 254: 115525.

Palmer, I. D. Induced stresses due to propped hydraulic fracture in coalbed methane wells. Paper SPE 25861 Presented at the SPE Rocky Mountain Regional/Low-Permeability Reservoirs Symposium, Denver, Colorado, 12-14 April, 1993.

Potluri, N. K., Zhu, D., Hill, A. D. The effect of natural fractures on hydraulic fracture propagation. Paper SPE 94568 Presented at the SPE European Formation Damage Conference, Scheveningen, The Netherlands, 25-27 May, 2005.

Ren, L., Yu, Z., Zhao, J., et al. Hydraulic fractures simulation in non-uniform stress field of horizontal shale gas well. Journal of Petroleum Science and Engineering, 2022, 216: 110843.

Rocha, J. A. L., Wahrhaftig, A. M. Superposition of stress fields in diametrically compressed cylinders. Latin American Journal of Solids and Structures, 2016, 13(10): 1954-1967.

Shi, S., Wang, M., Tang, W., et al. Study of stress field induced by natural fracture and its influence on hydraulic fracture propagation. Journal of Petroleum Exploration and Production Technology, 2024, 14(4): 1085-1099.

Sun, R., Huang, D., Chen, D., et al. Research on casing failure mechanisms and countermeasures in hydraulic fracture of shale reservoirs considering dynamic evolution of fault slip. Engineering Failure Analysis, 2024, 161: 108301.

Sun, T., Zeng, Q., Xing, H. A quantitative model to predict hydraulic fracture propagating across cemented natural fracture. Journal of Petroleum Science and Engineering, 2022, 208: 109595.

Tan, P., Chen, Z., Fu, S., et al. Experimental investigation on fracture growth for integrated hydraulic fracturing in multiple gas bearing formations. Geoenergy Science and Engineering, 2023, 231: 212316.

Teixeira Silveira, B., Roehl, D., Mejia Sanchez, E. C. Forecasting of the interaction between hydraulic and natural fractures using an artificial neural network. Journal of Petroleum Science and Engineering, 2022, 208: 109446.

Warpinski, N. R., Branagan, P. T. Altered-stress fracturing. Journal of Petroleum Technology, 1989, 41(9): 990-997.

Xia, Y., Wang, Y., Yang, H., et al. Studies on mechanical properties and failure characteristics of anisotropic shale under true triaxial loading at real-time high temperature. Rock Mechanics and Rock Engineering, 2025, 58(7): 7203-7234.

Yang, R., Gong, Y., Shi, W., et al. Oriented perforation strategies for hydraulic fracturing in deep coalbed methane horizontal wells. SPE Journal. 2026, 31(4): 2467-2488.

Zeng, F., Guo, J. Optimized design and use of induced complex fractures in horizontal wellbores of tight gas reservoirs. Rock Mechanics and Rock Engineering, 2015, 49(4): 1411-1423.

Zhang, B., Fang, J., Ding, Y., et al. Determination of minimum *in-situ* stress from normalized Mohr-Coulomb failure criteria. Petroleum Exploration and Development, 2003, 30(6): 89-91.

Zhang, J., Yin, S. Fracture gradient prediction: An overview and an improved method. Petroleum Science, 2017, 14(4): 720-730.

Zhang, M., Zhou, K. R., Li, C., et al. Evolution of natural fracture stability in middle-deep shale reservoirs. Petroleum Science Bulletin, 2026, 11(1): 99-113. (in Chinese)

Zhao, C., Li, J., Liu, G., et al. Analysis of well stress with the effect of natural fracture nearby wellbore during hydraulic fracturing in shale gas wells. Journal of Petroleum Science and Engineering, 2020, 188: 106885.